AIAA AVIATION Forum
12-16 June 2023, San Diego, CA and Online
AIAA AVIATION 2023 Forum
10.2514/6.2023-4248

High-Speed Imaging of Interaction of Liquid Drops with Hypersonic Projectiles

A. R. Dworzanczyk*, J. D. Langhorn†, and N. J. Parziale‡
Stevens Institute of Technology, Hoboken, New Jersey 07030, USA

C. J. Croft§, D. R. Wise¶, and M. A. Libeau‖
Naval Surface Warfare Center Dahlgren Division, Dahlgren, Virginia, 22448, USA

Water drops were suspended in the flight path of high-speed projectiles fired by the Naval Surface Warfare Center Dahlgren Division's (NSWCDD's) electromagnetic launcher (EML) located at the Hypersonic Research and Integration for Surface Engagement (HYRISE) facility at the Potomac River Test Range. Drops of diameter 1-3 mm were suspended in place using acoustic levitators and backlit with a pulsed laser synchronized to a high-speed Kirana camera. This enabled aerobreakup study at high Weber number (5e4-4e5), Mach number (1.5-1.9), and Reynolds number (6e4-3e5). We found that non-dimensional drop-diameter increase and drop acceleration were consistent with previous drop breakup studies. Mass shedding and breakup behavior are also consistent with previous drop breakup studies. Drop deformation consistent with what we believe to be Rayleigh-Taylor piercing was observed for certain cases where the instability wavelength was long enough to be captured with the current experimental setup. Drop-remnant/projectile collision was found to result in high-speed radial liquid jetting that appears to drive a shock wave radially from the impact location. Drop-remnant/projectile collision also results in a shock propagating in a direction normal to the projectile surface.

I. Nomenclature

a	=	Acceleration
C_D	=	Drag Coefficient
d_d	=	drop diameter
λ	=	wavelength
m_d	=	drop mass
μ	=	viscosity
Oh	=	Ohnesorge number
ρ	=	density
ρ_d	=	drop density
Re	=	Reynolds number
σ	=	Surface Tension
T	=	Non-Dimensional Time
t	=	time
t_c	=	Characteristic breakup time
u	=	velocity
We	=	Weber number
X	=	Non-Dimensional Displacement

*Graduate Student, Mechanical Engineering, 1 Castle Point on Hudson, Hoboken, New Jersey 07030.
†Graduate Student, Mechanical Engineering, 1 Castle Point on Hudson, Hoboken, New Jersey 07030.
‡Associate Professor, Mechanical Engineering, 1 Castle Point on Hudson, Hoboken, New Jersey, 07030, AIAA Associate Fellow.
§Mechanical Engineer, Integrated Engagement Systems Department, Dahlgren, Virginia, 22448, USA.
¶Mechanical Engineer, Integrated Engagement Systems Department, Dahlgren, Virginia, 22448, USA.
‖Hypersonic Technology Chief Scientist, Integrated Engagement Systems Department, Dahlgren, Virginia, 22448, USA.

II. Introduction

High-speed vehicle design requires the consideration of many fundamental fluid-mechanic phenomena [1]. Researchers often isolate poorly-understood flow physics and devise experiments and computations with the hope of constructing useful models. For example, consider the decades-long efforts and rich community focused on high-speed boundary-layer instability and transition [2–4]. Analogous to the important fundamental problem of instability is the interaction of high-speed vehicles with natural weather.

High-speed-vehicle/rain-encounter is a rich, underexplored, multiphase fluid-mechanics problem where the droplets can appreciably deform prior to impact. Impacts with droplets or small particles at high velocity can degrade aerospace materials, reducing transparency and other desirable properties [5, 6]. The length scales of the droplets involved can be on the order of the grain size of a material, reducing the utility of a material's bulk properties for estimating the scope of this potential damage [7, 8], while both the sphericity and size of a droplet can change the degree of damage in a collision [7]. At the same time, the interaction of the shock structure around a vehicle can disrupt a droplet, potentially altering the deleterious effects of impact [9–11]. Therefore, it is important to develop a fundamental understanding of droplet deformation and impact.

In Pilch and Erdman [12], droplet breakup is discussed as a series of different breakup regimes corresponding to increasing aerodynamic force on the liquid drop. As the ratio of aerodynamic force to restoring capillary force on the drop increases (nondimensionalized as Weber number, We), the drop is said to pass from bag to bag-and-stamen to stripping to catastrophic breakup regimes. These regimes are described by Waldman and Reinecke [13], Waldman et al. [14], Reinecke and Waldman [15], and Simpkins and Bales [16]. In this understanding of droplet breakup, the development of edge stripping from the droplet occurs at lower values of We, while at very high values of We, Rayleigh-Taylor surface waves are said to grow in an unstable and exponential manner until their amplitude is comparable to the droplet diameter, triggering catastrophic drop disintegration. This model of droplet breakup appeared to be supported by high-speed shadowgraph images generated by Reinecke and Waldman [15], which showed catastrophic disintegration only at Weber numbers above $4e4$, but showed stripping behavior at lower We.

Theofanous et al. [17] presents an alternative droplet breakup model, describing liquid drop breakup behavior as having two distinct regimes depending on Weber number (We). The first, occurring at a lower Weber number ($We < 10e3$), involved Rayleigh-Taylor surface instability waves that grow in magnitude until the drop structure is pierced and distorted. This regime was dubbed "Rayleigh-Taylor Piercing" (RTP). At the lowest Weber numbers in this regime, surface waves are comparable in amplitude to droplet diameter, producing the phenomena that earlier studies described as "bag" breakup. Starting from about $We = 1e3$, and as We becomes arbitrarily large, the regime transitions to Shear-Induced Entrainment (SIE). As We increases, the wavelength of surface waves generated through Rayleigh-Taylor instability (RTI) decreases, and shear stress on the liquid surface grows. When We reaches values of $1e4$ to $1e5$, RTP ceases to be a significant feature in drop breakup entirely [17]. Theofanous and Li [18] assert that by using Laser-Induced Fluorescence (LIF), they conclude that the apparent large-amplitude surface waves in earlier "catastrophic" breakup images were merely mirages produced by the shadowgraph imaging method, and noting that the very high post-shock temperatures in the high Mach number flows studied by Reinecke and Waldman [15] impose a substantial thermal load on the water droplets that may produce effects distinct from mechanical breakup.

In this work, we study the flow structure in the stagnation region of a high-speed projectile during an encounter with a liquid droplet. The projectile is launched from an electromagnetic railgun at sea level at Mach number $M_\infty = 3.1 - 5.4$. Droplets of diameter 1-3 mm were suspended in place using acoustic levitators yielding Weber numbers in the range of $We = 5e4 - 4e5$. Time-resolved shadowgraphs are recorded which provide data on the shock structure, flow topology, and droplet deformation.

III. Facility and Experimental Setup

The experiments were performed at the Naval Surface Warfare Center Dahlgren Division's (NSWCDD's) electromagnetic launcher (EML) located at the Hypersonic Research and Integration for Surface Engagement (HYRISE) facility at the Potomac River Test Range located in Dahlgren, Virginia, USA [19]. The EML digitally prescribes projectile launch acceleration profiles so it provides a ground test capability with a broad range of precisely controlled velocities for weather encounters and terminal impacts with a launch cadence of multiple shots per day [20].

For this testing campaign, eight flat-faced, bore-rider projectiles were fired at velocities between 1000 m/s and 1900 m/s into a sea-level atmosphere. The projectiles were made of either aluminum or steel, depending on what permissions were given by the Potomac River Test Range on that day. The material of the projectile determines total shot energy which affects the intensity of the muzzle flash from the railgun. The flat-faced bore rider is approximately

100 mm wide by 150 mm tall. The ambient run conditions and projectile velocity for each of the eight shots are provided in Table 1, as is the calculated projectile Mach number relative to the ambient air.

Water droplets of diameter from 1 mm to 3 mm were suspended along the projectile's line of flight using acoustic levitators [21, 22]. A snapshot of the projectile traversing the acoustic levitator is seen in Fig. 1. The droplets were initially suspended in the middle of the levitator frame such that the droplet is processed along the approximate path of the stagnation streamline of the projectile. Alignment was performed with a Bosch laser sight and level. Misalignment from the path of the stagnation streamline is no more than 5 mm.

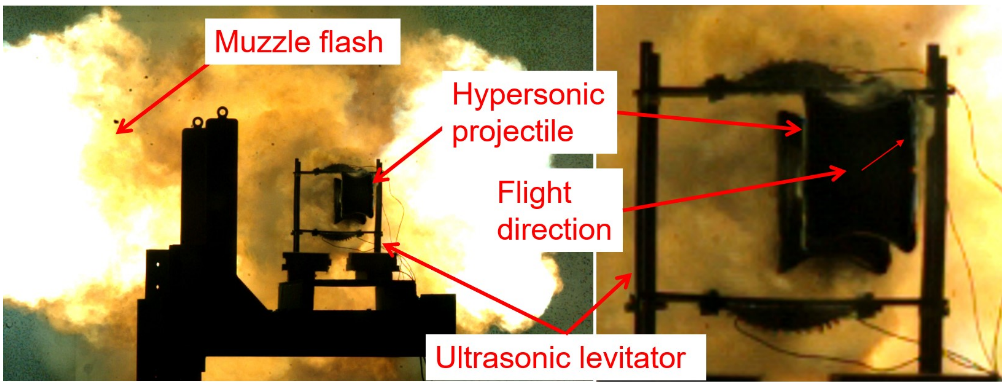

Fig. 1 NSWCDD projectile passing through the acoustic levitator frame. Projectile is approximately 100 mm x 150 mm. Droplet is initially suspended in the middle of the levitator frame such that the droplet is processed along the stagnation streamline of the projectile.

Shot (-)	Date (mm/dd/yy)	Velocity (m/s)	Temperature (K)	Mach Number (M_P)	Pressure (mb)	Humidity (%)	Energy (MJ)
22082401	08/24/2022	1040	302.6	2.97	1016.0	50	5.6
22082501	08/25/2022	1535	298.5	4.42	1017.5	58	12.2
22082601	08/26/2022	1083	300.2	3.11	1014.8	59	9.6
22092201	09/22/2022	1640	298.4	4.72	1005.8	72	13.5
22092202	09/22/2022	1864	296.5	5.38	1006.1	65	17.5
22092601	09/26/2022	1808	297.5	5.21	1009.1	50	26.2
22092602	09/26/2022	1797	298.5	5.18	1008.5	39	26.5
22092603	09/26/2022	1112	299.3	3.20	1007.4	37	10.1

Table 1 Ambient conditions and shot velocities for the current test campaign. Note the shot number is the Dahlgren convention of yy/mm/dd/number-that-day.

Backlit shadowgraphy and front-lit imaging [23, 24] were used to image the droplet. For the backlit shadowgraphy, the droplet-projectile interaction is illuminated from behind by a laser light source synchronized to the recording camera, in this case, a Kirana high-speed camera operated at 2-4 million frames per second (FPS). Backlit illumination was provided with two different lasers during this test campaign. For the first three shots, a Silux laser (Specialised Imaging) was synchronized to the Kirana camera, pulsing for 10 ns per frame. The next five shots were conducted 4 weeks later and the Silux laser was unavailable. The substitute light source chosen was an LDX-3230-685 fiber-coupled diode driven by an LDP v03-100 laser controller from PicoLas and collimated by a combination of ThorLabs fiber collimation package and a lens, similar to Parziale et al. [25]. The collimation optics and power rating of the second laser required the pulse duration to be increased to 100 ns to ensure sufficient illumination. For front-lit imaging, a Phantom TMX 7510 camera was run at 300,000 FPS, also with 100 ns exposure time, and the light source was the railgun's own muzzle flash (Fig. 1).

A schematic drawing of the experimental setup at the railgun facility is provided in Fig. 2. A liquid droplet of a diameter between 1 and 3 mm is suspended using an acoustic levitator in the path of a projectile fired from the railgun.

Precision trigger timing is required because the Kirana camera can record only 180 frames. This results in 90 µs and 45 µs of recording time for 2M FPS and 4M FPS, respectively. To achieve precision timing, a laser interrupt trigger was devised consisting of a 532 nm laser pointer, a DET36A2 biased photodetector fitted with a 532 nm bandpass filter to block muzzle flash, and an oscilloscope. When that beam is interrupted by the projectile, the falling edge signal from the photodetector triggers the oscilloscope's output, which triggers a pulse generator, in turn triggering the high-speed cameras. Trigger timing could be prescribed down to less than 5 µs from laser interrupt.

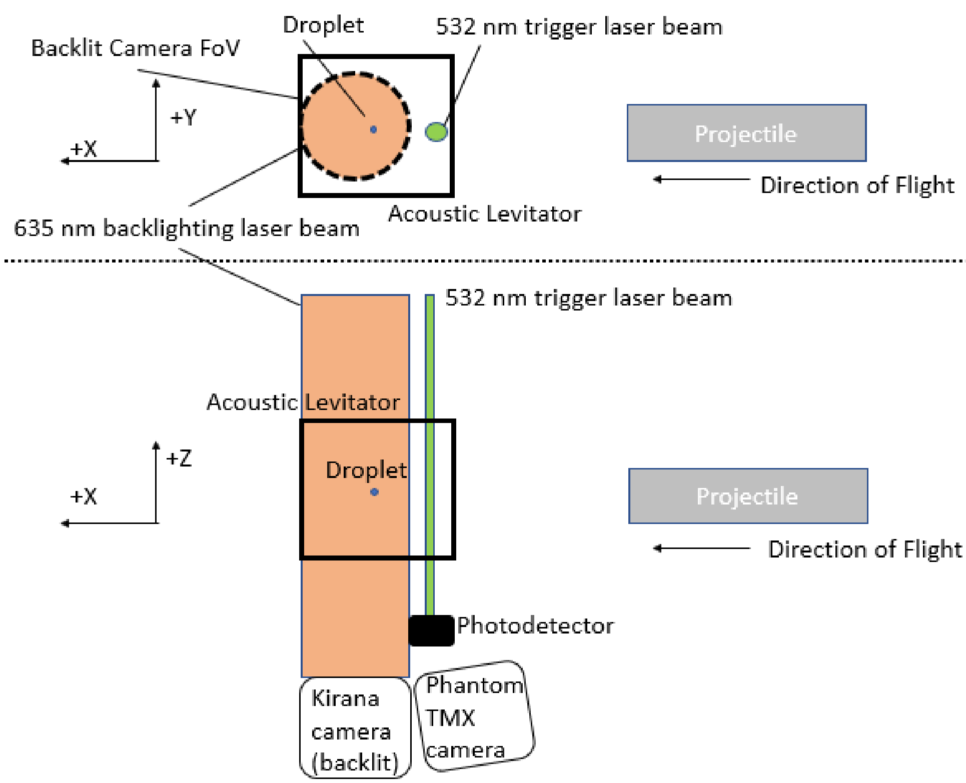

Fig. 2 Schematic of experimental setup. Projectile interrupts green trigger laser beam, which causes the high-speed cameras to begin recording. Kirana camera is backlit by 635 nm laser beam. Phantom TMX is front-lit by flash from railgun muzzle. A drop is suspended on projectile flight line by an acoustic levitator.

IV. Droplet Aerobreakup and Flow Topology

In this section, the flow around the drop before impacting the projectile face is discussed. To determine the conditions of the gas surrounding the drop during aerobreakup, we assume that the conditions in the stagnation region are constant. We estimate these conditions by calculating the post shockwave state assuming thermochemical equilibrium using Cantera [26] with the Shock and Detonation Toolbox [27]. We acknowledge this is a crude assumption and this will be revisited in future work. Fig. 3 shows the four compressible gas states of interest during this experiment campaign. State 1 is the state of the undisturbed ambient air. State 2 is the state of the air disrupted by the projectile bow shock. State s is the state of the air at the stagnation region on the projectile's face; as stated, these conditions are assumed to be approximately equal to those in State 2. State 2' is the state between the levitated drop and its own bow shock; it is air that is processed by two consecutive planar bow shocks.

The non-dimensional numbers of interest are

$$We = \frac{\rho u^2 d_d}{\sigma}, \quad (1)$$

$$Oh = \frac{\mu_d}{\sqrt{\rho_d d_d \sigma}}, \quad (2)$$

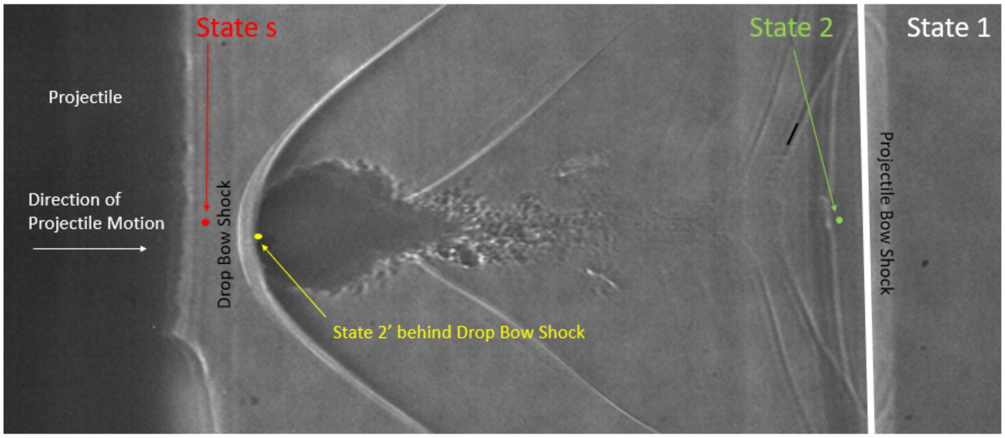

Fig. 3 Four states of air of interest in this experiment campaign: State 1, undisturbed air; State 2, the gas immediately following the projectile bow shock; State s, air at projectile stagnation point; State 2', air immediately behind the drop bow shock.

$$Re = \sqrt{\frac{We}{Oh}}, \tag{3}$$

and

$$T = \frac{t}{t_c} = t/\left(d_d \frac{\sqrt{\rho_d/\rho_\infty}}{u_\infty}\right), \tag{4}$$

where t_c is a characteristic breakup time defined by Reinecke and Waldman [15], among others. For each drop, the non-dimensional values are tabulated in Table 2. The Mach number is given for the projectile relative to the undisturbed air in state 1 (M_P), and the drop relative to the disturbed air in state 2 (M_d). We,Re,Oh, and t_c are also given relative to the disturbed air in State 2. These nondimensional parameters indicate that, in all cases, the inertial forces on a drop far exceeded viscous forces and surface tension.

Drop	Shot	Mach Number (M_P)	Mach Number (M_d)	We_2	Re_2	Oh_2	t_{c2} (µs)
2	22082501	4.42	1.75	$2.43e5$	$2.02e5$	0.0024	18.95
4	22092201	4.72	1.80	$1.83e5$	$1.39e5$	0.0031	10.92
5	22092201	4.72	1.80	$8.08e4$	$6.12e4$	0.0046	4.79
6	22092202	5.38	1.90	$4.43e5$	$2.80e5$	0.0024	15.27
7	22092601	5.21	1.88	$3.76e5$	$2.48e5$	0.0025	14.72
8	22092602	5.18	1.87	$4.18e5$	$2.79e5$	0.0023	16.88
9	22092602	5.18	1.87	$3.29e5$	$2.19e5$	0.0026	13.25
10	22092603	3.20	1.47	$8.77e4$	$1.20e5$	0.0025	30.47
11	22092603	3.20	1.47	$5.48e4$	$7.46e4$	0.0032	18.90

Table 2 Droplet Nondimensional Parameters and Characteristic Times

Firstly, Fig. 4 gives a comparison of a liquid drop processed by a bow shock wave to a hard sphere in a supersonic flow field famously reported in van Dyke [28]. Both the drop and the hard sphere generate a bow shock, but otherwise, there are substantial differences between the two flow fields. The hard sphere experiences boundary layer separation when its laminar boundary layer passes through an oblique shock roughly 90° away from the stagnation point. The most similar feature on the liquid drop takes place substantially farther downstream, near where the drop produces a teardrop-shaped tail. Because of the liquid drop's deformation and narrowing, the wake is substantially smaller relative to the size of the drop than it is for the hard sphere.

The evolution of Drop 7 from nondimensional time $T = 0$ to $T = 1$, is presented in Fig. 5. Because the post-shock flow is still supersonic with respect to the laboratory reference frame (and thus to the drops), each drop forms its bow

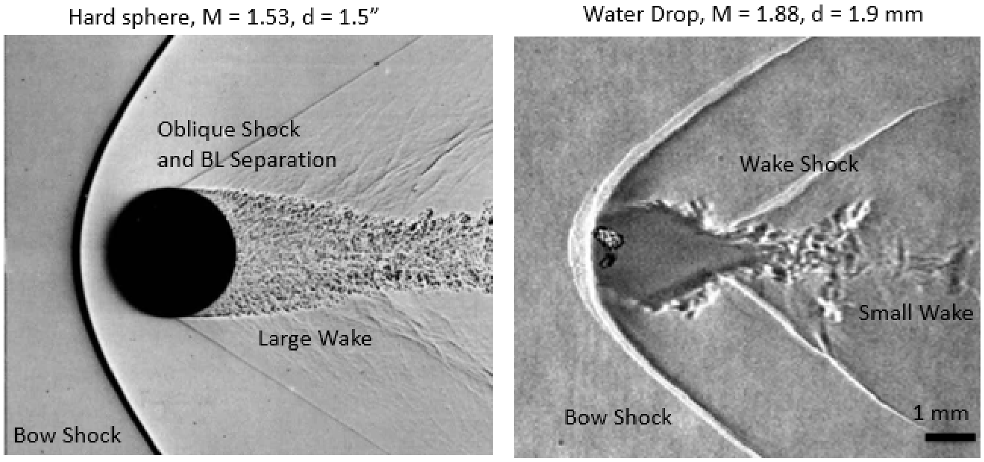

Fig. 4 Comparison of Drop 7 to Hard Sphere in Supersonic Flow Field from van Dyke [28].

shock within the post-shock flow field. At the same time, the drop appears to flatten and widen, indicating possible mist stripping from the edges of the drop. Such misting was detected as early as nondimensional time $T = 0.1$ by Hebert et al. [29]. The mist develops into a teardrop shape downrange of the drop, converging to a point. A wake shock forms roughly halfway down the length of the mist. Additionally, a fainter shock structure is visible between the drop and the projectile's bow shock. This final structure appears to be an indentation in the projectile's bow shock caused by the drop. This example was found to be typical of the drops imaged in this campaign.

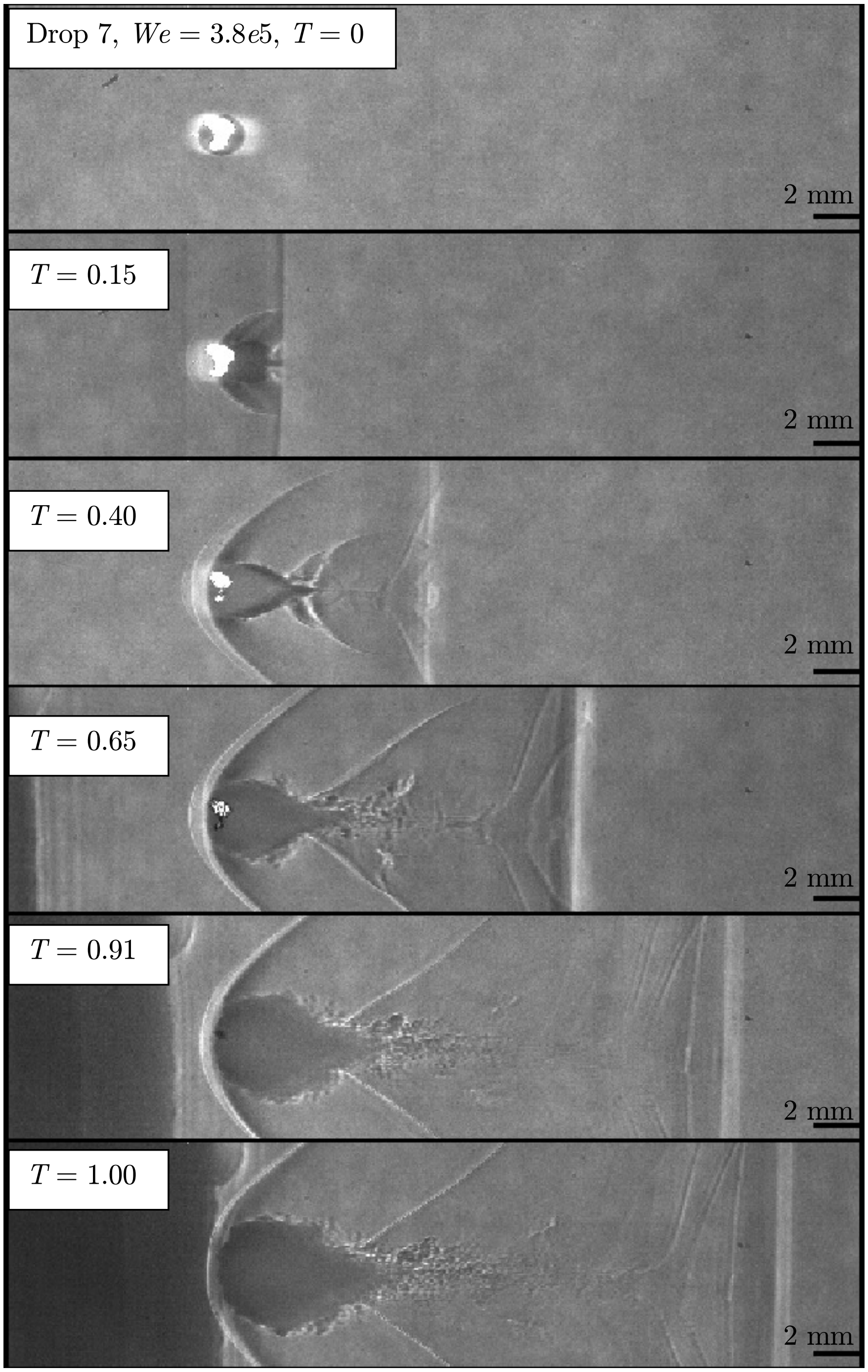

Fig. 5 Evolution of Drop 7 from initial frame to 1 t_c after shock interaction begins. The bow shock from the projectile is the nearly vertical line moving left-right across the page. The projectile is visible as the black mass from $T = 0.65 - 1.00$ on the left part of the page.

In Fig. 6, we present the flow topology at non-dimensional times 0.35 and 0.9 for 8 drops studied. As time progresses, the drops grow wider and the mist in their wakes grows longer. It also appears that at higher We, the drop is flatter and the tail of the drop shorter.

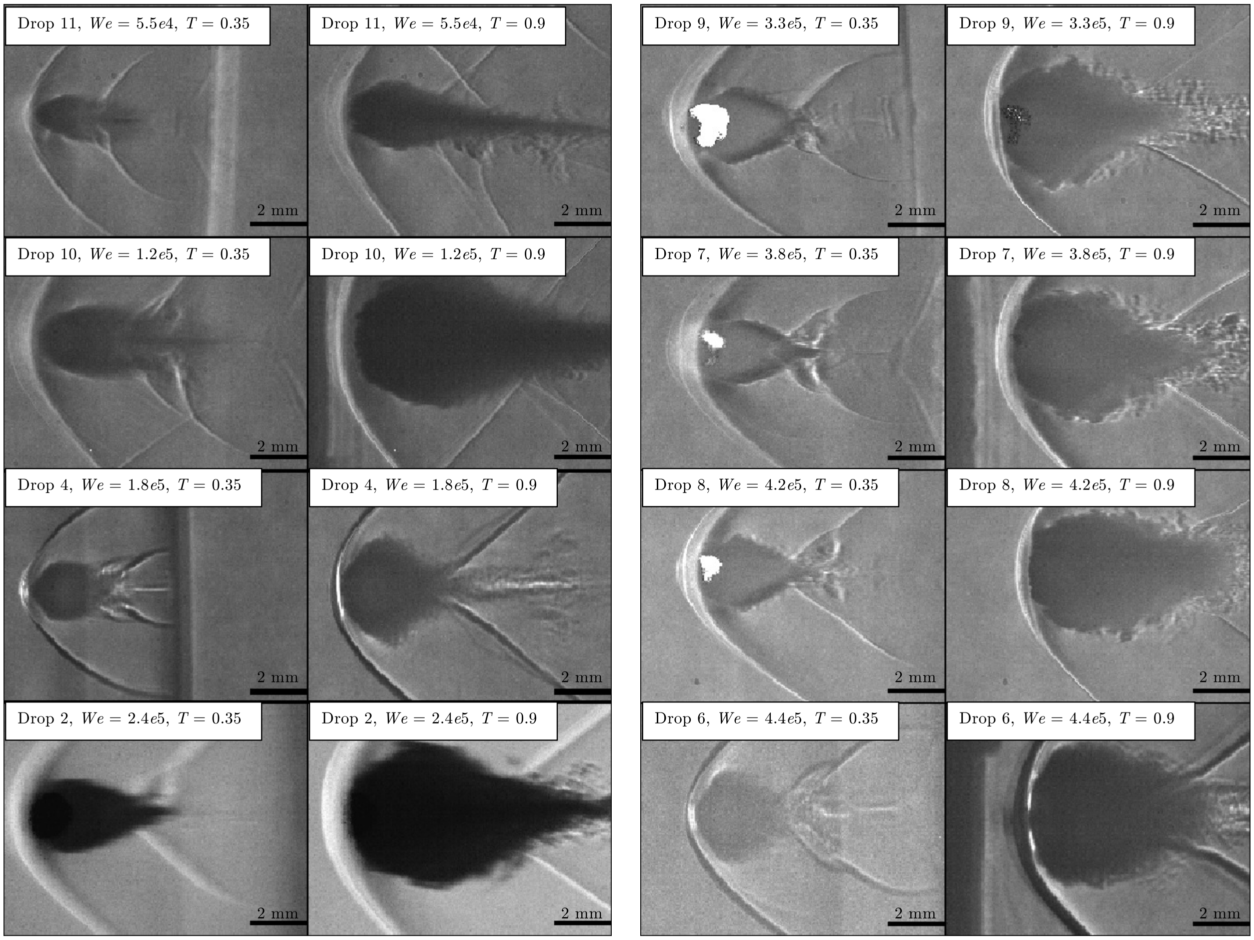

Fig. 6 All drops imaged at $T = 0.35$ and $T = 0.9$, showing similar, but not identical, flow morphologies at matching non-dimensional times.

The non-dimensional diameter of the drops (width divided by initial diameter) as a function of non-dimensional time (that is, actual time since shock interaction normalized by the calculated characteristic breakup time) is given in Fig. 7. Most of the drops grow linearly in Fig. 7 until impact with the incoming projectile. Drop 5, the smallest drop studied (diameter ≈ 500 µm), is seen to shrink until the end of the video of Shot 4. This drop initially grew larger in the same manner as the larger drops, but shear stripping consequently reduced its diameter again and again. The video of Shot 4 reveals that, from $T = 2$ to $T = 5$, the drop experiences mass stripping, with large volumes of water separating from the circumference of the flattened drop and accelerating rapidly away. Fig. 8 documents this process for Drop 5.

Fig. 7 shows that Drops 4 and 11 also experience mass stripping, though, for these larger drops, this phenomenon begins very shortly before projectile impact. Drop 4 reaches a maximum non-dimensional diameter of approximately 3, while drop 11 reaches a maximum non-dimensional diameter of approximately 4. Drop 5, previously discussed, also reaches a maximum non-dimensional diameter of approximately 3. Previous research in Hebert et al. [29] and Dworzanczyk et al. [30] also observed stripping when the non-dimensional diameter reached a value of 3. Whether some non-dimensional diameter value between 3 and 4 constitutes a critical size for drop mass shedding is under continuing analysis.

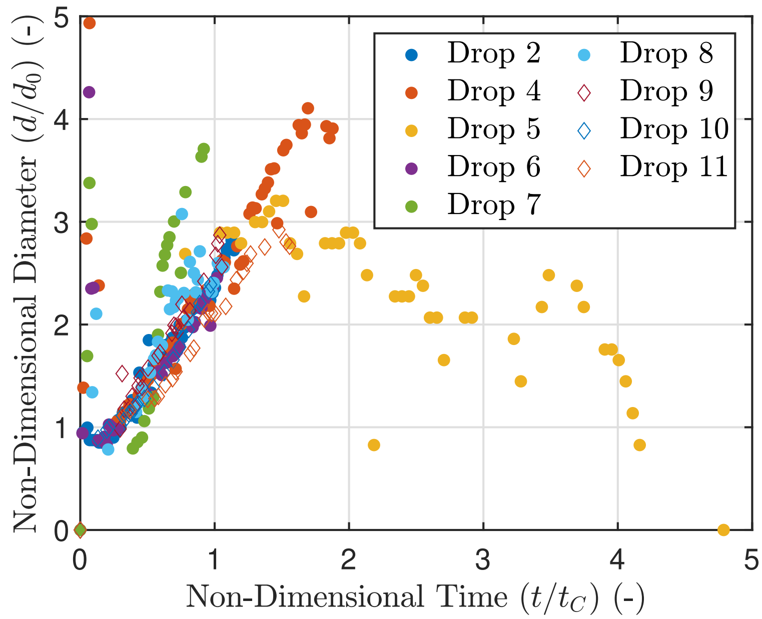

Fig. 7 Non-Dimensional Diameters of All Drops plotted against Non-Dimensional Time

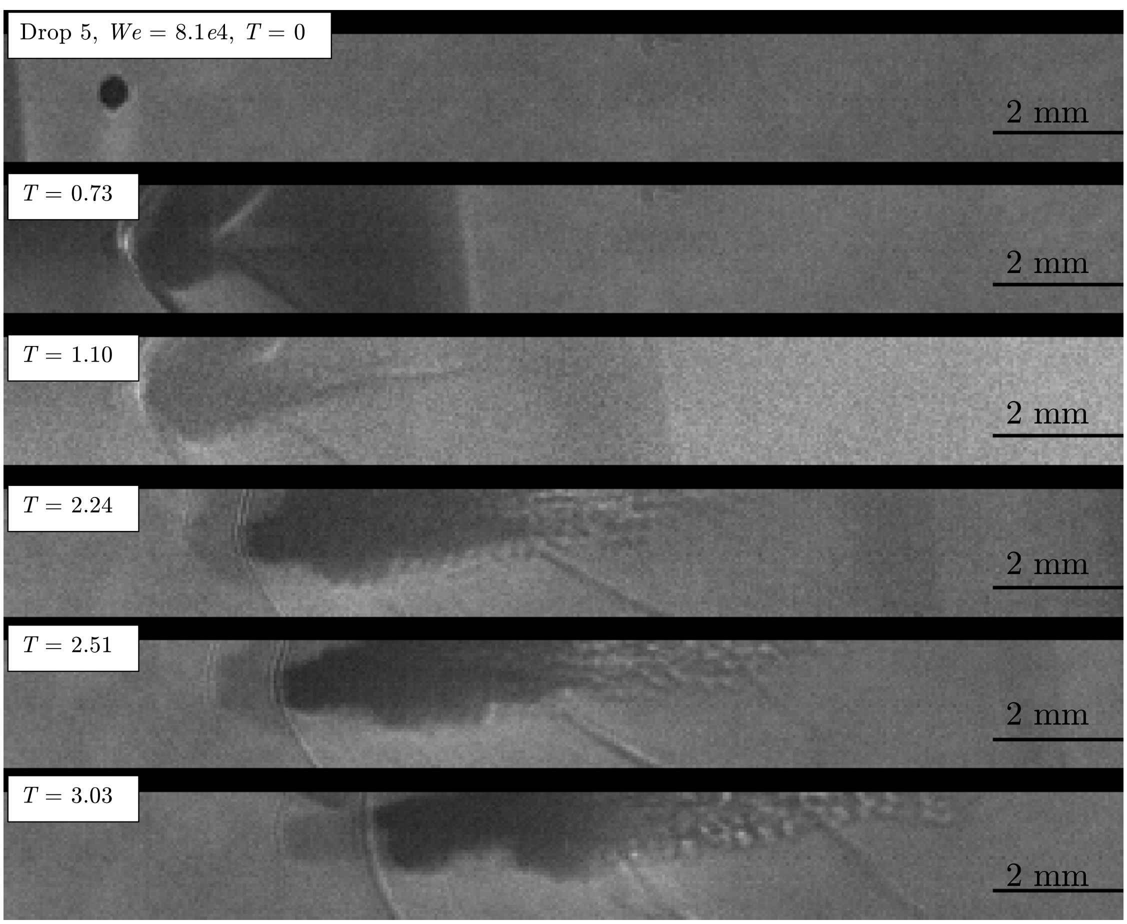

Fig. 8 Evolution of Drop 5 from initial condition to 3 t_c.

Drop 11 may provide an insight into the phenomena at play in the drop mass shedding process as a function of We. Shortly before its impact with the projectile, Drop 11's silhouette ceases to be teardrop-shaped, and instead takes on a sawtooth shape. The drop's silhouette can be compared between time $T = 0.9$ in Fig. 6 and time $T = 1.5$ in Fig. 9. At time $T = 0.9$, drop 11's silhouette remains teardrop-shaped and resembles the silhouette of Drop 10 (from the same shot) at the same non-dimensional time. By the time $T = 1.5$, however, the windward face of Drop 11 has become sawtooth-shaped, indicating the shedding of material away from the main body of the drop.

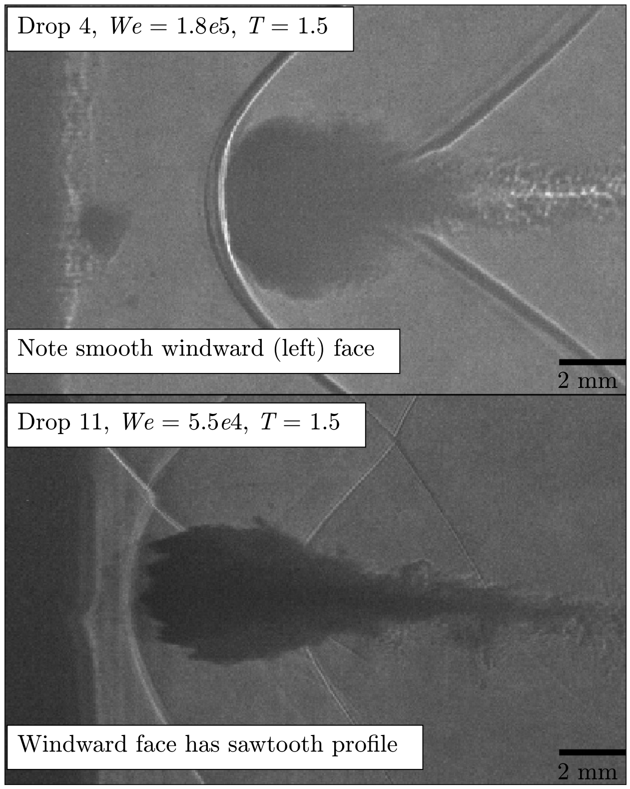

Fig. 9 Drops 4 and 11 at same T = 1.5, showing presence of sawtooth morphology at lower We.

Only 3 drops in this experiment campaign could be documented after time $T = 1$: Drops 4, 5, and 11. For Drop 5, the camera resolution is too small to determine whether the same phenomenon is present. Drop 4 does not appear to show the same sawtooth shape at a similar non-dimensional time but at higher We. The sawtooth morphology is not visible in the Drop 4 video, though some small rippling on the windward side may represent a similar phenomenon. Drop 4 experienced a much higher projectile velocity than Drop 11 (1640 m/s vs. 1112 m/s), and consequently has a higher Weber number ($1.83e5$ vs. $5.5e4$); though the Weber number only differs by a factor of 4 between Drops 4 and 11, this may be sufficient to place the drops in differing breakup regimes.

All the drops are seen to move from their initial location as a result of aerodynamic forces imposed by the incoming projectile. Smaller drops move more than larger ones, due to their lower mass. The displacement of the center of mass cannot be easily computed due to the mist obscuring the drop's center and possible distortion; the displacement of the drop bow shock is used as a proxy for the displacement of the drop's center of mass. The nondimensional displacement of each drop (displacement divided by initial diameter) is plotted against nondimensional time (up to values of 5) in Fig. 10. Drop 5 is a small drop and the tracking error may have made the initial location difficult to precisely note. In each plot of non-dimensional displacement, a theoretical displacement assuming a constant drop drag coefficient of 2 or 3 is plotted. Following Hebert et al. [29], a nondimensional displacement as a function of non-dimensional time is given as

$$X = \frac{3C_D T^2}{8}. \tag{5}$$

Prior research by Hebert et al. [29] found an approximate drag coefficient of 2.2 for liquid drops in conditions similar to those in this experiment. By comparing the displacements of the drops in this experiment to the theoretical displacements at a certain drag coefficient, it is possible to compare the drag coefficients to those found by Hebert et al. [29]. In this experiment, the non-dimensional displacements of the drops are consistent with a drag coefficient of this magnitude. Drops 7, 8, and 9 most clearly indicate a drag coefficient slightly less than 2, while drop 5 shows a higher drag coefficient than 3 until it begins shedding mass around nondimensional time 3.

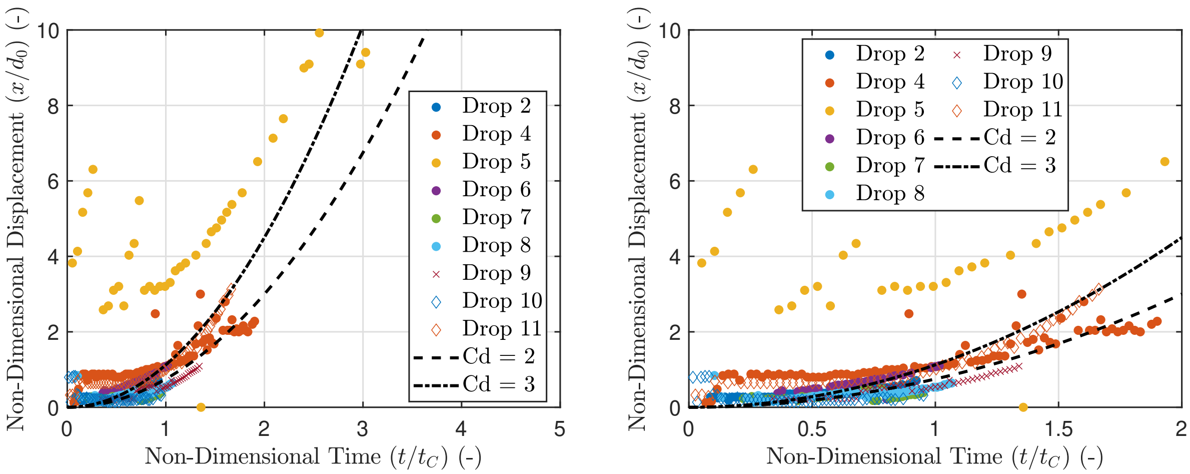

Fig. 10 Non-Dimensional displacement of all drops plotted against non-dimensional time. Right is zoomed in view of left.

Previous experiments have not reached a consensus on surface wave behavior and its role in drop breakup. Joseph et al. [31] and Reinecke and Waldman [15] reported observing Rayleigh-Taylor piercing (RTP). However, Theofanous and Li [18] suggested that "that the previously available experimental results, which are based on the shadowgraph method, allowed misinterpretations that have lead to inappropriate conceptualizations (and theory) of the physics that govern breakup at high Weber numbers ($We > 10^3$) — instead of the Rayleigh–Taylor piercing, the dominant mechanism is shear-induced motion with a significant radial component and instabilities on the so-generated, stretched liquid sheet." In an attempt to help address this question, the expected size of surface instability waves caused by both Rayleigh-Taylor (RT) and Kelvin-Helmholtz (KH) instability was estimated for the drops imaged in this experiment. From Sharma et al. [32], the wavelength for KH instability that corresponds to the maximum growth rate is given by

$$\lambda_{KH_{max}} = \frac{3\pi d_d}{We}, \tag{6}$$

which for cases here is calculated to be 200 nm or smaller. Also, from Sharma et al. [32], the wavelength for RT instability that corresponds to the maximum growth rate is given by

$$\lambda_{RT_{max}} = 2\pi\sqrt{\frac{3\sigma}{\rho_d a}}, \tag{7}$$

where a is the drop acceleration and is determined from data in Fig. 10 that is averaged for $T < 1$. Estimates of the RT and KH wavelengths are listed in Table 3. For Drop 11, which had the longest calculated RT wavelength of 77 µm, features of this wavelength appear on the windward face of the drop (Fig. 9). For the cases with $\lambda_{RT_{max}} \approx 30$ µm, smaller features may be able to be seen on the windward surface.

V. Future work on Droplet Impact

In this series of experiments, the droplets impact the projectile with varying degrees of demise. When the projectile impacts the drop remnant, the flow appears to demonstrate high-velocity radial jetting. We hypothesize that the jetting acts as a fluid piston and drives a radially-expanding shock. Additionally, a shock wave propagates normal to the projectile surface. This flow structure is defined in Fig. 11 and will be studied in future work.

Drop	We (-)	d_d (mm)	Acceleration (m/s^2)	λ_{RT} (µm)	λ_{KH} (nm)
2	$2.43e5$	1.847	$7.84e6$	33	71
4	$1.83e5$	1.163	$1.28e7$	25	60
5	$8.08e4$	0.512	$6.60e7$	11	59
6	$4.43e5$	1.953	$1.25e7$	26	41
7	$3.76e5$	1.805	$1.85e7$	22	45
8	$4.18e5$	2.049	$1.51e7$	24	46
9	$3.29e5$	1.610	$8.50e6$	32	46
10	$8.77e4$	1.805	$7.96e6$	33	194
11	$5.48e4$	1.122	$1.46e6$	77	193

Table 3 Calculated surface wavelengths

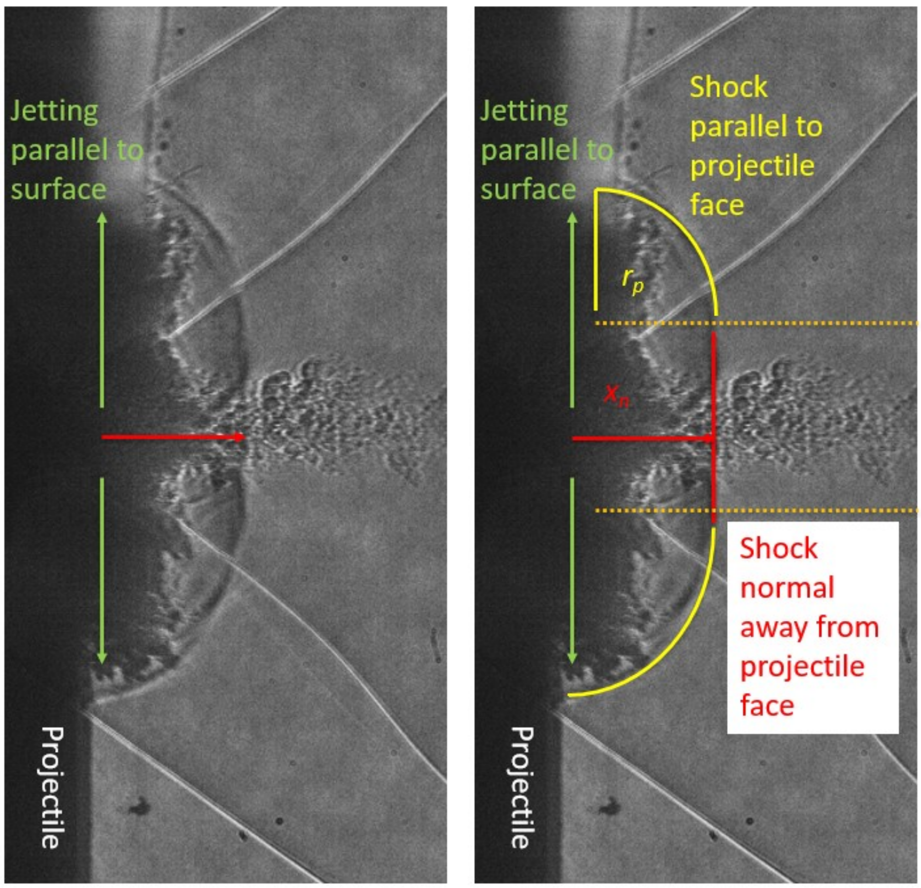

Fig. 11 Droplet impact for Drop 7. We show here radial jetting, a radially-propagating shock wave and a shock wave propagating normal to the projectile surface.

VI. Conclusion

Multiphase flow interactions between liquid droplets and a high-speed projectile were imaged using high-speed cameras. The high-speed projectile was fired from a railgun through an ultrasonic levitator that was used to suspend a single liquid drop at a precise location. Backlit shadowgraphy was used to image the high Weber/Reynolds/Mach number interactions.

Aerobreakup studies found that non-dimensional drop-diameter increase and drop acceleration were consistent with previous drop breakup studies. Mass shedding and breakup behavior are also consistent with previous drop breakup studies. Drop deformation consistent with what we believe to be Rayleigh-Taylor piercing was observed for certain cases where the instability wavelength was long enough to be captured with the current experimental setup. Drop-remnant/projectile collision was found to result in high-speed radial liquid jetting that appears to drive a shock wave radially from the impact location. Drop-remnant/projectile collision also results in a shock propagating normal to the projectile surface outward from it.

Future work will focus on characterizing and quantifying post-collision phenomena, and on further characterizing the Rayleigh-Taylor piercing phenomenon.

Acknowledgments

Dworzanczyk, Langhorn, and Parziale were supported by ONR-MURI Grant N00014-20-1-2682. Special thanks go to the staff of the Naval Surface Warfare Center railgun facility.

References

[1] Leyva, I. A., "The relentless pursuit of hypersonic flight," *Physics Today*, Vol. 70, No. 11, 2017, pp. 30–36. https://doi.org/10.1063/PT.3.3762.

[2] Johnson, H. B., Seipp, T. G., and Candler, G. V., "Numerical Study of Hypersonic Reacting Boundary Layer Transition on Cones," *Physics of Fluids*, Vol. 10, No. 13, 1998, pp. 2676–2685. https://doi.org/10.1063/1.869781.

[3] Schneider, S. P., "Development of Hypersonic Quiet Tunnels," *Journal of Spacecraft and Rockets*, Vol. 45, No. 4, 2008, pp. 641–664. https://doi.org/10.2514/1.34489.

[4] Fedorov, A., "Transition and Stability of High-Speed Boundary Layers," *Annual Review of Fluid Mechanics*, Vol. 43, 2011, pp. 79–95. https://doi.org/10.1146/annurev-fluid-122109-160750.

[5] Lapp, R. R., Stutzman, R. H., and Wahl, N. E., "A Study of Rain Erosion in Plastics and Metals," WADC 53-185, 1954.

[6] Moylan, B., Landrum, B., and Russell, G., "Investigation of the Physical Phenomena Associated with Rain Impacts on Supersonic and Hypersonic Flight Vehicles," *Procedia Engineering*, Vol. 58, 2013, pp. 223–231. https://doi.org/10.1016/j.proeng.2013.05.026.

[7] Adler, W. F., "Investigation of Liquid Drop Impacts on Ceramics," ETI-CR-82-1075, 1982.

[8] Adler, W. F., "Rain impact retrospective and vision for the future," *Wear*, Vol. 233-235, 1999, pp. 25–38.

[9] Reinecke, W. G., and McKay, W. L., "Experiments on Water Drop Breakup Behind Mach 3 to 12 Shocks," SC-CR-70-6063, 1969.

[10] Barber, J. P., Taylor, H. R., Grood, E. S., and Hopkins, A. K., "Water Drop/Bow Shock Interactions," AFML-TR-75-105, 1975.

[11] Barber, J. P., "Water Drop Breakup/Impact Damage Thresholds," AFML-TR-76-126, 1976.

[12] Pilch, M., and Erdman, C. A., "Use of breakup time data and velocity history data to predict the maximum size of stable fragments for acceleration-induced breakup of a liquid drop," *International Journal of Multiphase Flow*, Vol. 13, No. 6, 1987, pp. 741–757. https://doi.org/10.1016/0301-9322(87)90063-2.

[13] Waldman, G. D., and Reinecke, W. G., "Particle Trajectories, Heating, and Breakup in Hypersonic Shock Layers," *AIAA Journal*, Vol. 9, No. 6, 1971, pp. 1040–1048. https://doi.org/10.2514/3.6328.

[14] Waldman, G. D., Reinecke, W. G., and Glenn, D. C., "Raindrop Breakup in the Shock layer of a High-Speed Vehicle," *AIAA Journal*, Vol. 10, No. 9, 1972, pp. 1200–1204. https://doi.org/10.2514/3.50350.

[15] Reinecke, W. G., and Waldman, G. D., "A Study of Drop Breakup Behind Strong Shocks with Applications to Flight," AVSD-0110-70-RR, 1970.

[16] Simpkins, P. G., and Bales, E. L., "Water-drop response to sudden accelerations," *Journal of Fluid Mechanics*, Vol. 55, 1972, pp. 629 – 639.

[17] Theofanous, T. G., Li, G. J., and Dinh, T. N., "Aerobreakup in Rarefied Supersonic Gas Flows," *Transactions of the ASME*, Vol. 126, 2004, pp. 516–527.

[18] Theofanous, T. G., and Li, G. J., "On the physics of aerobreakup," *Physics of Fluids*, Vol. 20, No. 5, 2008, p. 052103. https://doi.org/10.1063/1.2907989.

[19] Tadjdeh, Y., "Navy's Electromagnetic Railgun Project Progressing," *National Defense*, Vol. 102, No. 764, 2017, pp. 33–34.

[20] O'Rourke, R., "Navy Lasers, Railgun, and Hypervelocity Projectile: Background and Issues for Congress," R44175, 2017. Congressional Research Service.

[21] Marzo, A., Barnes, A., and Drinkwater, B. W., "TinyLev: A multi-emitter single-axis acoustic levitator," *Review of Scientific Instruments*, Vol. 88, No. 8, 2017, p. 085105. https://doi.org/10.1063/1.4989995.

[22] Sheldon, R., "ParametricLev," , 2019. URL https://github.com/rsheldiii/ParametricLev, accessed: 2022-10-11.

[23] Settles, G. S., *Schlieren and Shadowgraph Techniques*, 1st ed., Springer-Verlag Berlin Heidelberg, 2001.

[24] Danehy, P. M., Weisberger, J., Johansen, C., Reese, D., Fahringer, T., Parziale, N. J., Dedic, C., Estevadeordal, J., and Cruden, B. A., "Non-Intrusive Measurement Techniques for Flow Characterization of Hypersonic Wind Tunnels," *Flow Characterization and Modeling of Hypersonic Wind Tunnels (NATO Science and Technology Organization Lecture Series STO-AVT 325)*, NF1676L-31725 - Von Karman Institute, Brussels, Belgium, 2018.

[25] Parziale, N. J., Schmidt, B. E., Damazo, J. S., Wang, P. S., Hornung, H. G., and Shepherd, J. E., "Pulsed Laser Diode for Use as a Light Source for Short-Exposure, High-Frame-Rate Flow Visualization," *Proceedings of AIAA SciTech 2015*, AIAA-2015-0530, Kissimmee, Florida, 2015. https://doi.org/10.2514/6.2015-0530.

[26] Goodwin, D. G., "An Open-Source, Extensible Software Suite for CVD Process Simulation," *Proceedings of CVD XVI and EuroCVD Fourteen, M Allendorf, F Maury, and F Teyssandier (Eds.)*, 2003, pp. 155–162.

[27] Browne, S., Ziegler, J., and Shepherd, J. E., "Numerical Solution Methods for Shock and Detonation Jump Conditions," GALCIT - FM2006-006, Caltech, 2006.

[28] van Dyke, M., *An Album of Fluid Motion*, Parabolic Press, 1982.

[29] Hebert, D., Rullier, J., Chevalier, J., Bertron, I., Lescoute, E., Virot, F., and El-Rabii, H., "Investigation of mechanisms leading to water drop breakup at Mach 4.4 and Weber numbers above 10^5," *SN Applied Sciences*, Vol. 2, 2020. https://doi.org/10.1007/s42452-019-1843-z.

[30] Dworzanczyk, A., Parziale, N. J., Mueschke, N. J., Grosch, D. J., and Bueno, P., "High-Speed Imaging of Droplet Impact on a Hypervelocity Projectile," *Proceedings of AIAA Scitech 2023*, AIAA-2023-0464, National Harbor, Maryland and Virtual Event, 2023. https://doi.org/10.2514/6.2023-0464.

[31] Joseph, D., Bélanger, J., and Beavers, G. S., "Breakup of a liquid drop suddenly exposed to a high-speed airstream," *International Journal of Multiphase Flow*, Vol. 25, 1999, pp. 1263–1303.

[32] Sharma, S., Singh, A., Rao, S., Kumar, A., and Basu, S., "Shock Induced Aerobreakup of a Droplet," *Journal of Fluid Mechanics*, Vol. 929, No. A27, 2021. https://doi.org/10.1017/jfm.2021.860.